Energetic neutral atoms at Mars
4. Imaging of planetary oxygen

S. Barabash and M. Holmström

Swedish Institute of Space Physics, Kiruna, Sweden

A. Lukyanov

Coventry University, Coventry, UK

E. Kallio

Finnish Meteorological Institute, Geophysical Research, Helsinki, Finland

[1]   Photoionization of the Martian oxygen exosphere/corona results in the production of planetary oxygen ions. The newborn ions start moving on cycloid trajectories determined by the electric and magnetic fields of the solar wind. The oxygen ions can then charge exchange with the neutral gases (H, H_2, and O) of the Martian exosphere and be converted to energetic neutral atoms (ENAs). Using the empirical model of the solar wind flow near Mars developed by *Kallio* [1996], we calculate the electric and magnetic fields in the interaction region and obtain the global distribution of the oxygen ions by solving the kinetic equation with source and sink terms. The distribution turns out to be highly asymmetrical with a factor of 1000 excess in the ion column density in the hemisphere to which the interplanetary electric field points. The majority of the oxygen ions within $2R_m$ planetocentric distances (R_m is the Martian radius) have energies below 6 keV because the typical size of the system is too small for acceleration to higher energies. About 50% of the oxygen ions experience the change-exchange process that produces ENAs. Making line of sight integration of the ion global distribution, oxygen ENA images for vantage points in the noon-midnight meridian plane are obtained. The morphology of the images clearly reflects the structure of the parent ion distribution. The majority of the oxygen ENAs have energy below 600 eV. For these energies the integral flux is up to 10^4 $cm^{-2}s^{-1}eV^{-1}$. The oxygen ENA differential fluxes are high and reach 10^5 $cm^{-2}s^{-1}sr^{-1}eV^{-1}$ in the energy range $0.1-1.7$ keV, which can easily be detected by modern ENA instrumentation. Planetary oxygen ENA imaging at Mars is therefore feasible. The total ENA flux observed at a single vantage point depends on the total amount of oxygen ions in the system and may be used to obtain the instantaneous total ion flux escaping the planet.   *INDEX TERMS:* 2780 Magnetospheric Physics: Solar wind interactions with unmagnetized bodies; 7837 Space Plasma Physics: Neutral particles; 6225 Planetology: Solar System Objects: Mars; 7843 Space Plasma Physics: Numerical simulation studies; *KEYWORDS:* solar wind-Mars interaction, energetic neutral atoms (ENA), charge exchange, ENA imaging

1.   Introduction

[2] Energetic neutral atoms (ENAs) are produced via charge exchange between singly charged ions and atoms of the neutral gas background. Because only a small fraction of the ion energy (< 1 eV) is lost in the charge-exchange collision for relative energies greater than 100 eV, the energetic ion, now transformed into an ENA, essentially retains both the energy and direction it had at the moment of neutralization. For energies higher than the escape one for a body in question, ENAs are essentially not affected by any forces and propagate like photons carrying information about the parent plasma. These messengers can be recorded by a direction-responsive instrument to obtain an image of a distant source [*Williams et al.*, 1992]. This technique is called ENA imaging and has been successfully proven for Earth's magnetosphere [*Roelof*, 1987; *Burch et al.*, 2001] to investigate the ring current and plasma sheet dynamics and energization as well as polar outflow. Apart from the Earth, ENA production has been considered for the Saturnian magnetosphere [*Amsif et al.*, 1997], the Mercury magneto-

sphere [*Barabash et al.*, 2001], and the Martian plasma environment [*Barabash et al.*, 1995; *Kallio et al.*, 1997; *Holmström et al.*, 2002; *Mura et al.*, 2002; *Lichtenegger et al.*, 2002]. ENA imaging provides a means of remote diagnosis of plasmas on a global scale and is thus a very attractive addition to any local plasma measurements. However ENA fluxes are given by line of sight integrals of ion differential fluxes which mimic spatial variations of the ion fluxes. This makes the interpretation of the images a far from straightforward task. Extensive simulation and modeling analysis are required to infer physically important information from qualitative and quantitative features of the images. The problem of ENA image inversion could be even more difficult for Mars than for the terrestrial conditions. The Earth's magnetic field organizes the plasma distributions in the inner magnetosphere in a way which can be relatively simply modeled. The field configuration in the near-Mars space is determined externally by the solar wind and internally by the conditions in the upper atmosphere and ionosphere. Moreover, any global magnetic field model will depend heavily on what interaction models are chosen.

[3] Mars does not have a dipole magnetic field but rather crustal magnetic anomalies [*Acuña et al.*, 1998] that affect the solar wind interaction, but only on a small scale. On the large scale the solar wind interacts directly with the Martian atmosphere/ionosphere. Since the plasma flows through the regions with high neutral densities, the charge-exchange process is very efficient, making Mars as well as other nonmagnetized atmospheric bodies such as Venus and Titan very bright ENA sources. The following basic plasma populations can experience charge-exchange processes with the Martian exosphere: the solar wind, the shocked solar wind in the magnetosheath, and the planetary ions originating from the ionization of the exosphere itself. *Kallio et al.* [1997], *Holmström et al.* [2002], and *Mura et al.* [2002] considered in detail ENAs originating from the solar wind. *Lichtenegger et al.* [2002] studied hydrogen ENAs originating from ionized and accelerated planetary hydrogen. In this report we investigate oxygen ENAs originating from the planetary oxygen ions.

[4] Atoms of the oxygen corona are ionized via photo-ionization, charge exchange, and electron impact ionization then start moving in the electric and magnetic fields of the solar wind, gaining energy that significantly exceeds the escape energy (2.1 eV). A fraction of these ions can charge exchange with the upper atmosphere gases resulting in the generation of oxygen ENAs. The majority of the ions leave the system and this provides an effective channel for the planetary material escape. It was observed on the PHOBOS mission that the scavenging of planetary ions by the solar wind may have resulted in the removal of about 1 m of surface water over 4.5 billion years [*Lundin et al.*, 1991]. More detailed studies [*Perez-de-Tejada*, 1992] that take into account the variability of the ionosphere through planetary history, give a much higher (about 30 m) equivalent depth of water which has escaped due to the solar wind interaction process. This would account for up to 30% of at least a 100 m equivalent water layer which may have existed on Mars during its warm and wet epoch [*McKay and Stoker*, 1989].

[5] Experimental studies of the ion escape are quite difficult because the spacecraft-based in situ measurements provide only the local flux of the oxygen ions along a spacecraft orbit. To evaluate the global escape one could use statistical methods provided that the spatial coverage is sufficiently dense. Only global observations can give the instantaneous ion flux escaping the planet and ENA imaging appears to be a very promising technique to do that. The ENAs detected by an ENA instrument will provide an image of the oxygen ion population which can be converted into the oxygen ion distribution function from which the instantaneous ion escape flux can be deduced. For some vantage points the escape could be estimated directly from the total ENA flux measurements. In this report we simulate the expected images of oxygen ENA to evaluate the fluxes and understand their morphology. We also study connections between the total outflow of oxygen ions and expected flux of oxygen ENAs. The study provides the basis for the planetary ion imaging via ENA to be performed on the Mars Express mission by the ASPERA-3 experiment (Analyzer of Space Plasmas and Energetic Atoms) [*Barabash et al.*, 1998]. The instrument carries two ENA imagers. The ENA sensor capable of separating hydrogen and oxygen will provide ENA images in the energy range 0.1–10 keV with an angular resolution of $5° \times 30°$ (full width at half maximum), the geometrical factor 6×10^{-3} cm^{2}sr, and efficiency 1%–50% depending on energy.

[6] To simulate an ENA image, one needs to incorporate three basic components: the global distribution of the parent ion flux, the neutral density profiles, and the energy-dependent cross sections of charge-exchange reactions. The ENA fluxes are then obtained by the line of sight integration of ion fluxes weighted by the neutral gas density and cross section. The cross sections are taken from laboratory measurements, and the neutral density profiles are available from corresponding models and satellite observations. To obtain the global oxygen ion distribution was a new task. While several studies have been performed to understand the oxygen ion trajectories by a test-particle approach [*Luhmann and Schwingenschuh*, 1990; *Lichtenegger and Dubinin*, 1998; *Kallio and Koskinen*, 1999] no comprehensive overview of the global O$^+$ ion distribution is available. The previous studies were mainly focused on the O$^+$ ion dynamics in the Martian tail and the comparison with the PHOBOS-2 data.

2. Neutral Densities and Charge-Exchange Cross Sections

[7] For this study the neutral density profiles for H and H$_2$ have been taken from *Krasnopolsky and Gladstone* [1996], and for O (thermal or cold), and O (nonthermal or hot) have been based on the profiles given by *Zhang et al.* [1993]. To make the calculations more relevant to the Mars Express mission we consider the solar minimum case only. Under the solar maximum conditions the hydrogen neutral density is lower due to increased thermal escape [*Krasnopolsky and Gladstone*, 1996] and corresponding ENA fluxes would be lower, too, because hydrogen makes the main contribution to the conversion of the ions into ENAs [*Holmström et al.*, 2002]. While the H, H$_2$, and O (cold) profiles were taken directly from *Krasnopolsky and Gladstone* [1996] and *Zhang et al.* [1993], the O (hot) profile (*Zhang et al.* [1993, Figure 5]; EUV = 1 case) was fitted by the Chamberlain distribution for heights above 500 km. This was done in order to obtain an analytical parameterized
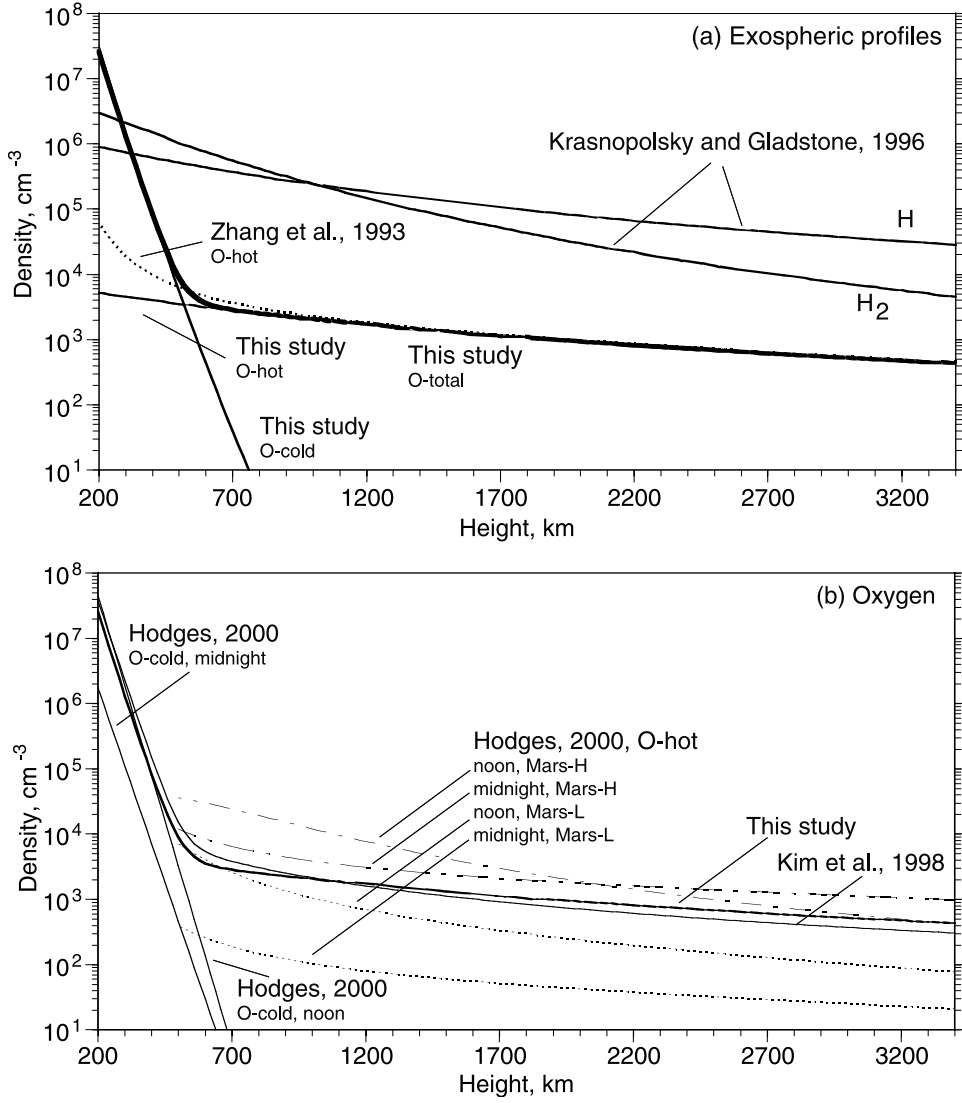
Figure 1. (a) Neutral gas profiles used in this study. The neutral density profiles for H and H_2 have been taken from *Krasnopolsky and Gladstone* [1996] and those for O-cold and O-hot have been adopted from *Zhang et al.* [1993]. (b) Comparison between different hot oxygen models.

expression which, on the one hand, accurately enough describes the hot oxygen distribution and, on the other hand, is simple enough to allow fast line of sight integration and parameter variations.

[8] Each neutral species density, n_i, was modeled by the Chamberlain distribution [*Chamberlain*, 1963]

$$n_i = n_i^0 \exp\left[H_i\left(\frac{1}{r} - \frac{1}{r_0}\right)\right]\zeta\left(\frac{H_i}{r}\right)$$

$$H_i = \frac{GMm_i}{kT_i}$$

(1)

where n_i^0 is the density at the exobase, $r_0 = R_m + 210$ km the exobase radius, T_i the temperature at the exobase, G the gravitational constant, M the mass of Mars, and m_i the atomic mass of the ith component. $\zeta(H_i/r)$ is the Chamberlain partition function which is not essential for the range of heights in question. Ionization processes such as photo-ionization and change-exchange will erode the above

distribution. This, however, takes place at such large distances that this oxygen population does not contribute significantly to the ion fluxes near the planet. Neither affects this remote population ENA generation because of its very low density. Figure 1a shows the neutral gas profiles used in this study and Table 1 summarizes the parameters, n_i and H_i, used in this study. The exospheric temperatures were around 200 K for H, 210 K for H_2 and O (cold), and 4650 K for O (hot). Note, that the expression (1) is very sensitive to H_i. As expected the hot oxygen profiles given by the expression (1)

Table 1. Exospheric Parameters Used in the Study[a]

Specie	Density, cm^{-3}	H_i, km
H	8.82×10^5	2.60674×10^4
H_2	2.89×10^6	4.95978×10^4
O(cold)	1.91×10^7	3.94227×10^5
O(hot)	5.16×10^3	1.78135×10^4

[a] From equation (1). All values are given for the height 210 km.

and by *Zhang et al.* [1993] become different for heights below 800 km. However, at around 600 km the cold oxygen density becomes considerable and the difference does not affect the total oxygen profiles, which differ only over the height range 600–800 km at most by 34%.

[9] Recently *Kim et al.* [1998] and *Hodges* [2000] reinvestigated the distributions of the hot (nonthermal) oxygen. Figure 1b compares these profiles with the one used in this study. For our distribution and the one from *Kim et al.* [1998] the sums of the hot and cold oxygen densities are shown. *Hodges* [2000] only provides the hot oxygen densities for altitudes above 500 km. His study takes into account the dependence of the hot oxygen distribution on the solar zenith angle and effects of the nighttime ionosphere. *Hodges* [2000] introduces two cases, Mars-L with no O_2^+ ions on the nightside, and Mars-H with the nighttime ionosphere constrained by *Fox et al.* [1993]. The profile used in this study is very close to the one given by *Kim et al.* [1998] for solar minimum. The difference is about a factor of 1.8 at most. The cold oxygen profile at noon given by *Hodges* [2000] is even closer to the one we use. Two models, Mars-L and Mars-H, introduced by *Hodges* [2000] set a rather wide range of the hot oxygen densities above 500 km. Our profile, adopted from *Zhang et al.* [1993] who considered the subsolar point, turned out to be right in between the Mars-L and the Mars-H cases at noon. In our model of the neutral oxygen distribution we disregard the solar zenith effects and assume the same distributions on the dayside and nightside. This does not introduce any significant errors in the oxygen ion density because photoionization operates, in any case, on the dayside only. It may, however, cause an overestimation of the ENA flux originating from the ions convected to the nightside. The proper modeling of the solar zenith effects can only be done through Monte Carlo simulations. However, for this study we would need a simplified model, which can be analytically fitted and readily incorporated into line of sight integrals, which give ENA fluxes. Results of Monte Carlo simulations presented in such a form are not available, so we were forced to use for these initial studies the simplified analytical expressions (1) with the parameters defined in Table 1.

[10] Figure 2 shows the charge-exchange cross sections for the reactions used in this work:

$$O^+ + O \rightarrow O + O^+$$
$$O^+ + H \rightarrow O + H^+$$
$$O^+ + H_2 \rightarrow O + H_2^+$$
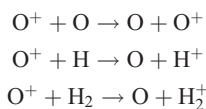
[11] The cross section for the first reaction was taken from *Torr et al.* [1974] for energies above 1 keV and assumed to be constant 2.03×10^{-15} cm^2 for 0.1–1 keV, thus underestimating the cross section because resonance charge-exchange cross sections increase with decreasing energy. The analytical fits (Chebyshev polynomials) for the last two reactions were taken from *Phaneuf et al.* [1987]. We did not consider helium in our analysis because the charge-exchange cross section for the reaction $O^+ + He \rightarrow O + He^+$ is smaller than 2×10^{-16} cm^2 for energies below 10 keV [*Phaneuf et al.*, 1987]. The energy range used in this study is 100 eV–10 keV, corresponding to the energy band of the available instrumentation for ENA measurements. As will be seen
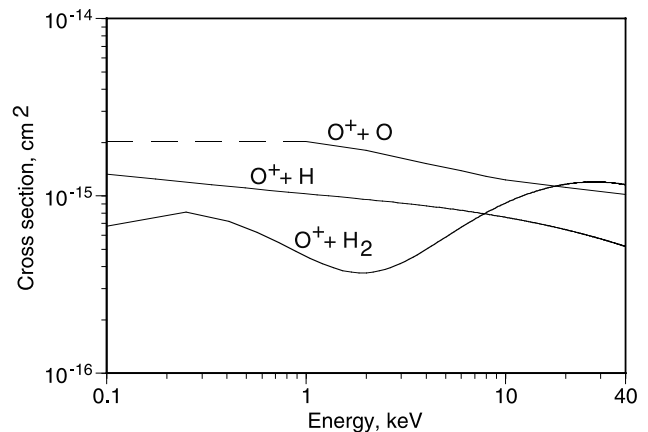
Figure 2. Cross sections for the charge-exchange reactions considered in the calculations. The cross section for the reaction $O^+ + O$ is extrapolated by the constant shown by the dashed line.

later, this range covers the most important part of the oxygen ion distribution function.

[12] Since the resonant charge exchange has larger cross sections than the other charge-exchange reactions, one may ask whether or not a significant moment transfer occurs in this collision. Indeed, during the resonance collision an oxygen ion and atom become indistinguishable and we do not know whether or not the outgoing oxygen ENA originates from the exosphere as a result of a knock-on collision or if it comes from the accelerated oxygen ion, that became neutralized. However, this is not important as long as a significant scattering does not occur. Recently *Lindsay et al.* [2001] published the differential cross sections for charge-exchange scattering in the reaction $O^+ + O$ for the energies 0.5–5 keV that is very close to the energy range 0.1–10 keV in question. As one can see in their Figure 2 the differential cross section's distributions over the entire range are highly peaked at 0°. For 500 eV the probability for ENA to be scattered by an angle of 0.2° is an order of magnitude smaller than an angle of 0.01°. These numbers are much below any feasible angular resolution that will be achieved even in future ENA instruments. Therefore, we can assume that the momentum transfer is insignificant for our consideration.

3. Global Oxygen Ion Distribution

[13] We assume that the O^+ ions result from ionization of the Martian oxygen corona. After ionization the ions are picked up by the solar wind electric and magnetic fields, are accelerated above the escape energy (2.1 eV), and leave the planet.

[14] In our calculations we use the magnetic field model based on the empirical model of the proton flow developed by *Kallio* [1996]. In this model the proton plasma flow lines are modeled to fit the PHOBOS/ASPERA three-dimensional measurements. Then, from the frozen-in condition, the magnetic field vector is calculated assuming it is known in the undisturbed solar wind; three magnetic field components around the planet are derived by calculating how the areas of three test surfaces deform when the surfaces that are initially perpendicular to each other in the solar wind flow

around the planet in the selected velocity model [see *Kallio*, 1996, equation (12)]. The consequence of the frozen-in condition is that the magnetic flux through the test surface **dA** remains unchanged and, therefore, that the value of the magnetic field component along the area surface vector **dA**/|**dA**|, B_i, is inversely proportional to the area of the test surface: $B_i \propto 1/|\mathbf{dA}|$.

[15] Following the frozen-in condition the electric field is given as $\mathbf{E} = -(\mathbf{v} \times \mathbf{B})/c$ where **v** is the local plasma velocity given by the flow model by *Kallio* [1996], **B** the magnetic field and c the speed of light. This model is an empirical one and based on measurements. The other models used for similar studies [*Luhmann and Schwingenschuh*, 1990; *Lichtenegger and Dubinin*, 1998] are based on a gas dynamic approach. For the simulations we assume that the solar wind magnetic field B_{sw} is equal to 2 nT and directed along the *OY* axis. The solar wind velocity V_{sw} is directed along the $-X$ axis and is equal to 500 km/s that is within the range 400–600 km/s measured by PHOBOS/ASPERA [*Kallio et al.*, 1994]. The corresponding convection electric field is along the *OZ* axis and is equal to 1 mV/m. A singly charged particle gains an energy of 3.4 keV traveling a distance of one Martian radius in this field.

[16] The initial neutral oxygen distribution is as described above. For this analysis we take into account only photoionization. Since the spatial distributions of the charge exchange and electron impact ionization rates are strongly model-dependent we do not consider these two processes. Therefore our calculations give lower limits of the oxygen ion and ENA fluxes. We do not consider the ion population resulting from the ionization (photoionization or stripping) of the oxygen ENAs, assuming that its contribution to the total ion density is negligible. This process, however, may result in high energy peaks on the energy distributions as observed in the cometary case [*Goldstein et al.*, 1987].

[17] To obtain the global distribution of the O^+ ions we use the kinetic approach and compute the distribution function $f(\mathbf{r}, \mathbf{v})$ for these ions in six-dimensional phase space. The simulation box is $4 \times 4 \times 4 \; R_m$ in physical space. Here **r** is the position, **v** is the ion velocity and $R_m = 3390$ km is the radius of Mars. The overall steps for computing the distribution function are:

1. The Lorentz force on the ions is computed by using **E** and **B** fields derived from the empirical proton flow model (described above).

2. The ion trajectories in (**r**, **v**)-space are determined by integration of the equations of motion.

3. The initial O^+ distribution given by the photoionization source is propagated along the trajectories.

4. The O^+ distribution function in each cell of the phase space is defined.

[18] Along ion trajectories in phase space the distribution function obeys the inhomogeneous Vlasov equation,

$$\frac{df}{dt} = S_i(\mathbf{r}, \mathbf{v}) + S_{ex}(\mathbf{r}, \mathbf{v}), \tag{2}$$

where the first term in the right hand side is the source of ions due to photoionization

$$S_i = f_N(\mathbf{r}, \mathbf{v})/\tau_i, \tag{3}$$

where f_N is the distribution function of neutral oxygen, a sum of the distribution functions for the cold and hot oxygen components. The photoionization time is τ_i and we have assumed that a produced ion has the same velocity as the original neutral. We used $\tau_i = 10^7$ s, corresponding to solar minimum conditions. The number was adjusted from the ionization time 4.16×10^6 s given for 1 AU at solar minimum by *Torr and Torr* [1985]. The second term describes the loss process due to charge-exchange reactions,

$$S_{ex}(\mathbf{r}, \mathbf{v}) = -\sum_k N_k(\mathbf{r})f(\mathbf{r}, \mathbf{v})v\sigma_k(v), \tag{4}$$

where the velocity magnitude $v = |\mathbf{v}|$, $N_k(\mathbf{r})$ is the neutral density of the kth species of the exosphere (O-hot, O-cold, H and H_2), and σ_k gives the cross sections for O^+-neutral charge exchange as shown in Figure 2. Here we have ignored the velocity of the neutrals compared to the ion velocity.

[19] When solving (2) we proceed as follows. First we consider the photoionization term only. Integrating along a trajectory, starting with $f = 0$ at $t = 0$, gives

$$f(t) = \int_0^t f_N(\mathbf{r}(t'), \mathbf{v}(t'))/\tau_i \, dt', \tag{5}$$

where we have used the notation $f(t) = f(\mathbf{r}(t), \mathbf{v}(t))$. Since the neutral oxygen energies given by the exospheric temperatures [*Zhang et al.*, 1993], 0.02 eV (210 K) and 0.40 eV (4650 K) for the cold and hot components respectively, are substantially lower than the oxygen ion energies, we can disregard the effects of the neutral gas distribution on the ion distribution. We thus approximate f_N by its average value $N(\mathbf{r})/v_T^3$ for $v < v_T$ and assume it to be zero for $v > v_T$. Here v_T is the neutral oxygen thermal velocity. If the time spent in the phase box $v_T \times v_T \times v_T$ (where f_N is nonzero) is τ_l, we can simplify the general equation (5),

$$f(t) \approx \int_0^{\tau_l} N(\mathbf{r}(t'))/v_T^3/\tau_i \, dt'$$

$$\approx N(\mathbf{r})_{t=0}/v_T^3\tau_l/\tau_i. \tag{6}$$

Here we have also assumed that $N(\mathbf{r})$ does not change much while the ion moves inside the velocity space box $v_T \times v_T \times v_T$ ($v < v_T$). The time τ_l is determined numerically by following the trajectory until $v > v_T$.

[20] In deriving (6), we have made several approximations that need to be justified. The ion energies greatly exceed the primary neutral oxygen energies, since the electric field quickly accelerates newly created ions to super-thermal energies, essentially separating the neutrals and the ions into different regions in phase space. That $N(\mathbf{r})$ is regarded as constant in (6) can be justified by considering that in an electric field of 1 mV/m (typical value in the simulations) an ion gains the energy 0.4 eV (corresponding to the thermal energy for the hot oxygen corona) over a distance of 400 m which is much smaller than the typical scale height. This also justifies not including charge exchange in the velocity space box, since the mean free path for an ion is more than 500 km; we deal with an "ENA-thin" medium.
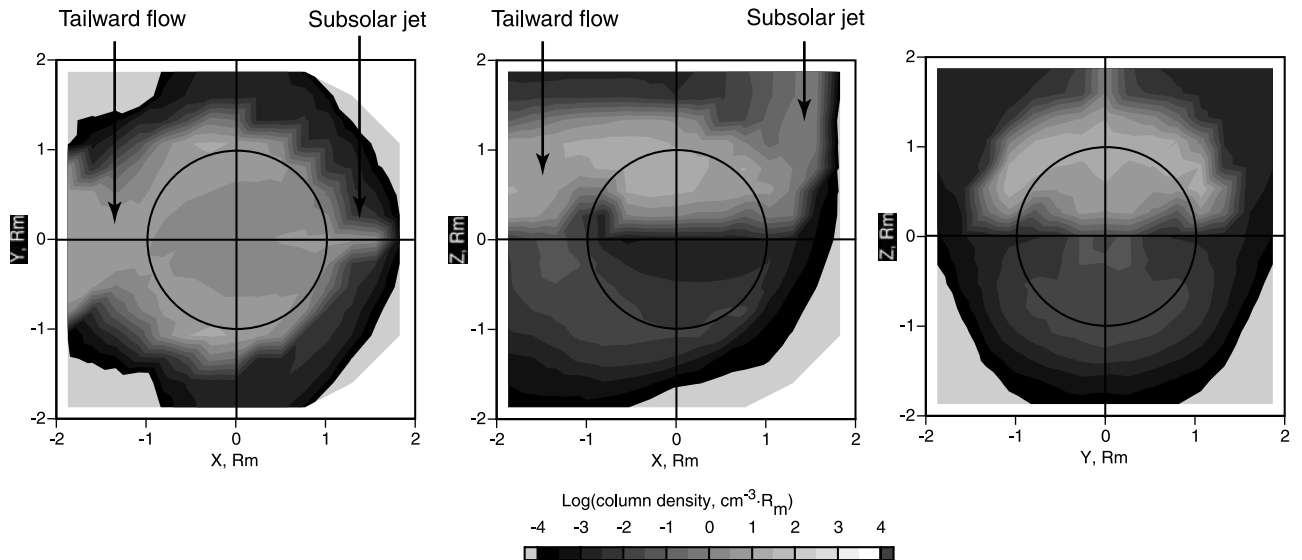
Figure 3. Oxygen ion column density distribution in the units $cm^{-3} \times R_m$ (3.39×10^8 cm^{-2}) in solar ecliptic coordinates. The solar wind magnetic field is 2 nT and directed along the OY axis. The corresponding convection electric field is along OZ. The solar wind velocity is directed along the $-X$ axis and is equal to 500 km/s. See color version of this figure at back of this issue.

[21] In summary, using (6), the photoionization source can be accounted for as an initial condition when solving (2) along a trajectory for the steady state distribution,

$$\frac{df}{dt} = S_{ex}(\mathbf{r}, \mathbf{v}) \quad (7)$$

$$f(\mathbf{r}, \mathbf{v})_{t=0} = f_0(\mathbf{r}) = N(\mathbf{r})_{t=0} / v_T^3 \tau_l / \tau_i.$$

The solution of (7), using (4), is

$$f(t) = f_0(\mathbf{r}) e^{-\int_0^t v \sum_k N_k \sigma_k dt'}. \quad (8)$$

The integral is taken along the particle trajectory which is determined by the usual equations of motion

$$\begin{cases} \frac{d\mathbf{r}}{dt} = \mathbf{v}, \\ \frac{d\mathbf{v}}{dt} = q/M(\mathbf{E} + (\mathbf{v} \times \mathbf{B})/c), \end{cases} \quad (9)$$

where $q = 1e$ is the ion charge and $M = 16$ amu the ion mass.

[22] From (8) we have the distribution function, $f(\mathbf{r}, \mathbf{v})$, along any trajectory. To compute f on a grid in the phase space we proceed as follows. Initial points in physical space, $\mathbf{r}$ at $t = 0$, are chosen on a spherical symmetric grid, with variable grid size over the radius to account for the exponential decay of the neutral oxygen density. The points are chosen randomly. The probability of being placed in a certain cell is proportional to the ion production rate there which, in our case, is proportional to the neutral oxygen density. The directions in velocity space are chosen randomly. We solve (8) along the ion trajectory and deposit the computed values of the distribution function in all grid cells that the trajectory passes through. When several trajectories go through the same cell, the average value of the distribu-

tion functions, weighted for the time spent in the cell, is stored. The phase space grid used to store the distribution function is rectangular with $15 \times 15 \times 15$ grid points in the physical space, and spherical with $10 \times 15 \times 15$ grid points in the velocity space. A total of 150 000 particles were launched in the simulation.

[23] To visualize the calculated distribution function we integrate it over the energy and one of the spatial variables to obtain the column density. Figure 3 shows the column density in the unit $cm^{-3} \times R_m$, which can be simply interpreted as an averaged density over one Martian radius, in solar ecliptic coordinates. A very strong asymmetry in the distribution between the $+Z$ and $-Z$ hemispheres results from the absorption of the ions born in the $-Z$ hemisphere when they are accelerated toward the planet by the electric field. The other important feature is a jet of ions originating near the subsolar point which moves almost parallel to the $+Z$ axis. The tailward flow in the $+Z$ hemisphere is also visible. These features and how they appear on oxygen ENA images will be discussed in the Discussion section.

[24] To understand the ion energies involved, we integrate the distribution function over all spatial variables and the solid angle in the velocity space. The spectrum (Figure 4) is expressed in the total number of particles per 1 eV. It drops sharply at energies less than 1 keV and rather hard between 1 and 6 keV. Above 6 keV the spectrum is cut off. This shape has a simple explanation. Due to the lack of room, the majority of particles cannot be accelerated to energies higher than 1 keV before they impact the planet. The particles which do not impact the planet can only be accelerated up to a maximum of 6 keV over a distance of $2R_m$. In principle, the ion energy can reach the maximum value $64E_{sw} = 83$ keV, where E_{sw} is the solar wind proton energy (1.3 keV in our case) provided there is sufficient room. However this population is not of importance for the ENA studies because the ions reach energies above 10 keV over distances larger than $2R_m$ where the neutral density is small. The ions which are
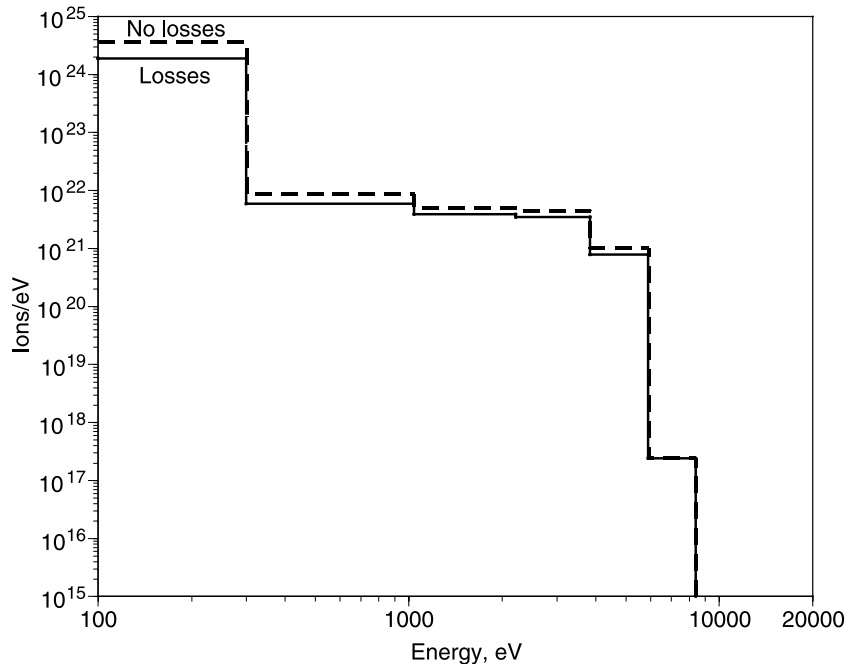
Figure 4. The oxygen ions near Mars distributed by energy. The two distributions correspond to the cases with the charge-exchange loss included (solid line) and not included (dashed line) in the calculations.

brought to the vicinity of the planet from the upstream region have very low fluxes and the fraction of such ions is negligibly small by comparison with the number of ions in the system. In Figure 4 we also show the spectrum calculated for the case when no loss via charge exchange is present, i.e. $S_{ex}(\mathbf{r}, \mathbf{v}) = 0$. Integrating the difference between two spectra over energy, one can establish that the charge-exchange process decreases the number of ions in the system by 48%, i.e. ENA production is very effective. However not all of the ENAs produced can be used for imaging because a large part of them hit the Martian surface.

4. ENA Images of Oxygen Ions

[25] Multiplying the distribution function with the ion momentum squared, we obtain the O^+ differential fluxes in each cell of our simulation box. Assuming that the ENA attenuation due to electron stripping is small since the cross section for this process is smaller than the resonance charge exchange [*Torr et al.*, 1974], we get for the ENA differential flux, $j_{ena}(\mathbf{r}, E_0, \mathbf{u})$, from the direction $\mathbf{u}$ at the vantage point $\mathbf{r}$ at the energy E_0,

$$j_{ena}(\mathbf{r}, E_0, \mathbf{u}) = \sigma(E_0) \int_0^\infty ds\, N(\mathbf{r} - s\mathbf{u}) j_{ion}(\mathbf{r} - s\mathbf{u}, E_0, \mathbf{u}), \quad (10)$$

where $\sigma(E_0)$ is the energy-dependent charge-exchange cross section, $N(\mathbf{r} - s\mathbf{u})$, and $j_{ion}(\mathbf{r} - s\mathbf{u}, E_0, \mathbf{u})$ the total neutral density and the ion differential flux at the point of the ENA generation. The integration is performed along the line of sight s. We chose four vantage points within the noon-midnight meridian. All points are at the $3R_m$ planetocentric distance and 45°, 90°, 135°, and 180° solar zenith angle (SZA). We chose this distance to relate our studies with the upcoming Mars Express mission which will have an

apocenter around $3R_m$. Figure 5 shows the vantage points and the corresponding ENA images in the fish-eye projection for different vantage points. The projection is a polar one, with the radius being the angle to the axis pointing toward the planetary center and the polar angle the angle to the solar direction in the plane perpendicular to the planetary center direction. The chosen energy range is 0.1– 1.65 keV to cover the main oxygen ion population (see Figure 4) and still make the result relevant to the available ENA instrumentation which has the lowest energy threshold around 100 eV. Within the chosen energy band we do not integrate the fluxes over energy but sum them up to keep the differential flux units. The angular resolution for the line of sight grid was 2.5° and 5°. The integration step was 20 km, i.e. much less than the scale height in question. The field of view is 120° to cover the entire interaction region. Apart from the four vantage points described above, we run simulations for vantage points on the $+Y$ axis at a distance of $3R_m$. Very weak ENA fluxes have been detected and we do not show this image. This is a consequence of the fact that the ion trajectories there are aligned with the electric field and corresponding ENAs are emitted within the directions close to the *OXZ* plane. As expected, ENA emissions are concentrated close to the planetary surface where the neutral density is highest, reflecting also the strong asymmetry observed in the ion distribution.

[26] Figure 6 shows the oxygen ENA spectra obtained by integration of the images in Figure 5 over the solid angle 2π. The integrated fluxes reach 10^4 cm^{-2}s^{-1}eV^{-1}. The majority of ENAs have energies below 600 eV.

5. ENA Flux and Ion Outflow

[27] Using the oxygen ion distribution function one can readily obtain the total flux of ions escaping the system by
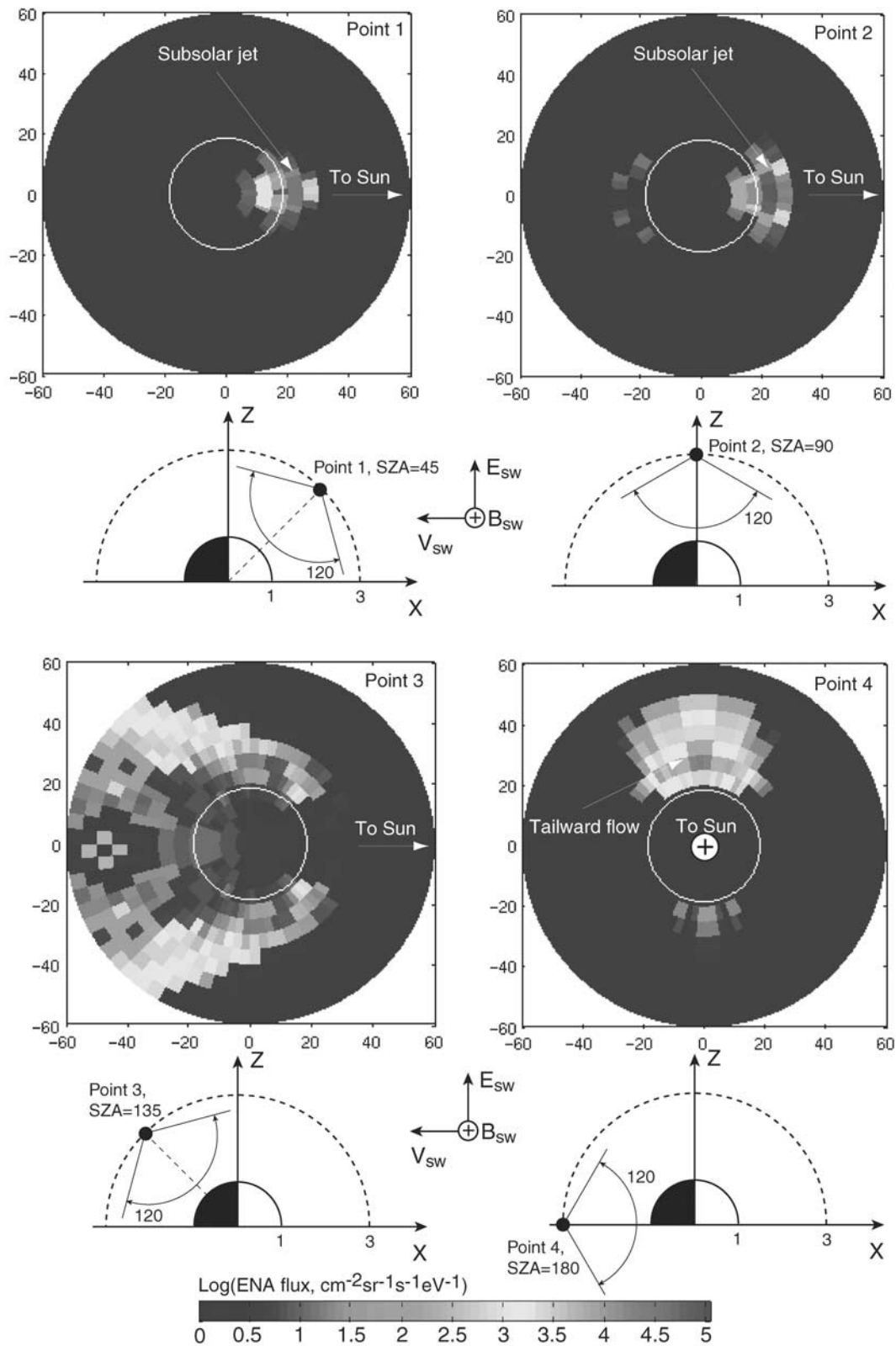
Figure 5. ENA images for vantage points with different solar zenith angles (SZA). The energy range: 0.1–1.65 keV. The position of the vantage points are shown in the inserts as well as electrical and magnetic field vectors. All points are in the *OXZ* plane. See color version of this figure at back of this issue.
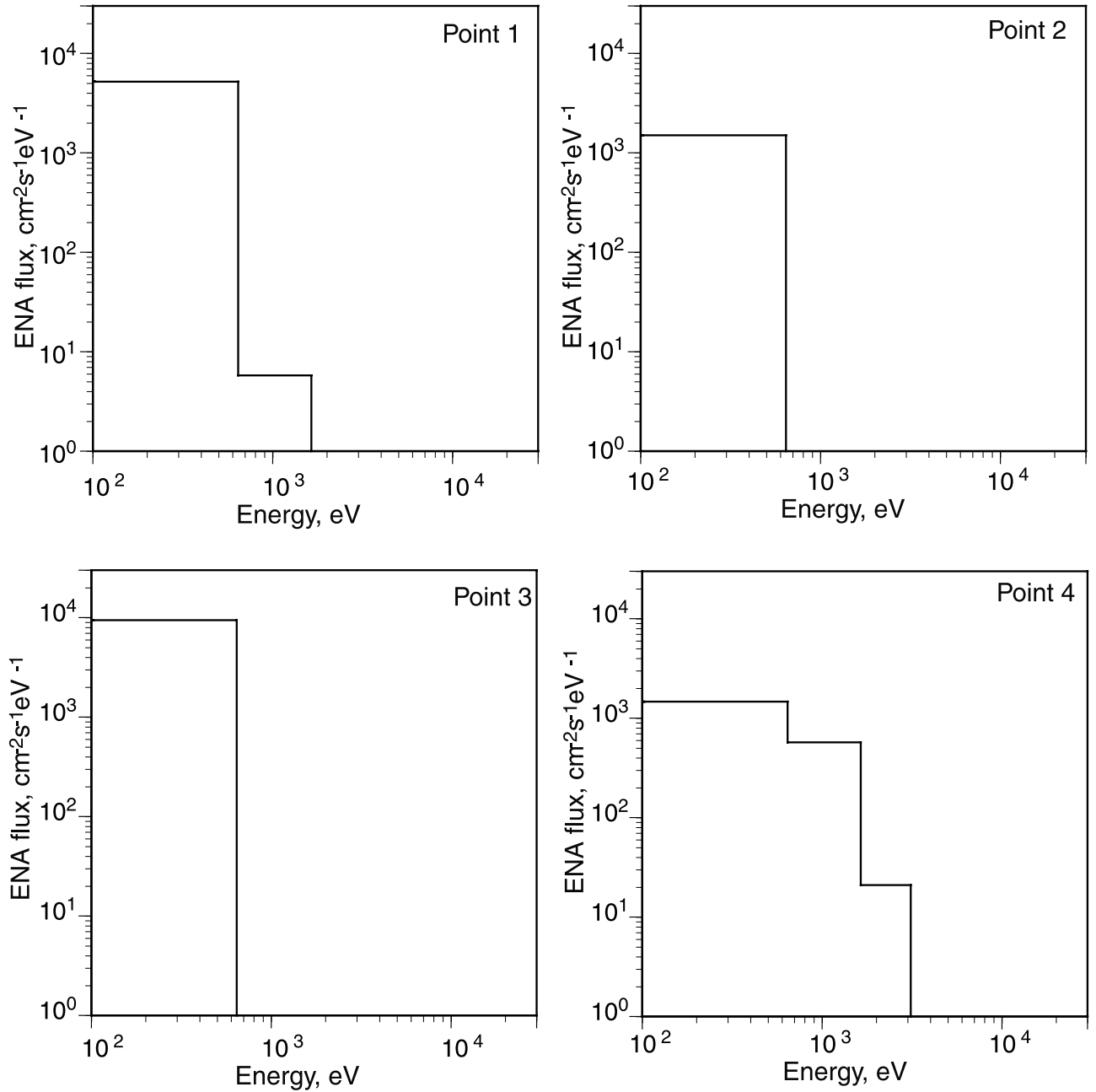
Figure 6. Oxygen ENA energy spectra for the vantage points shown in Figure 5. The majority of the ENAs have energies below 600 eV.

integrating the ion flux through the boundaries of the simulation box. In our case we obtained the rate 4.6×10^{24} s^{-1}. This is in good agreement with rates measured by different instruments on the PHOBOS mission. Indeed, *Rosenbauer et al.* [1989] and *Lundin et al.* [1989] give 2×10^{25} s^{-1} and *Verigin et al.* [1991] 5×10^{24} s^{-1} for the total escape rate. The spread in the experimental data comes from different assumptions on the target area the oxygen ions are escaping through. In our analysis we use only the photoionization channel for ion production and thus underestimate the total outflow flux. The difference in the solar conditions for the PHOBOS mission and Mars Express may also affect the comparison.

[28] In order to investigate the relations between the total ion outflow and the ENA flux emerging from the system, we vary the neutral oxygen gas distribution slightly by changing the oxygen exospheric temperature by 20% and compute the total ENA flux (cm^{-2}s^{-1}) for each vantage point in question. The total ENA flux is given by integration of the differential fluxes shown in Figure 5 over energy and solid angle 2π. We increase and decrease the exobase temperature around the nominal value for both hot and cold oxygen components. Surprisingly, the variation in the hot component does not affect the total ion outflow in any notable manner nor change the expected ENA fluxes. In contrast, the variation in temperature of the cold (or ther-
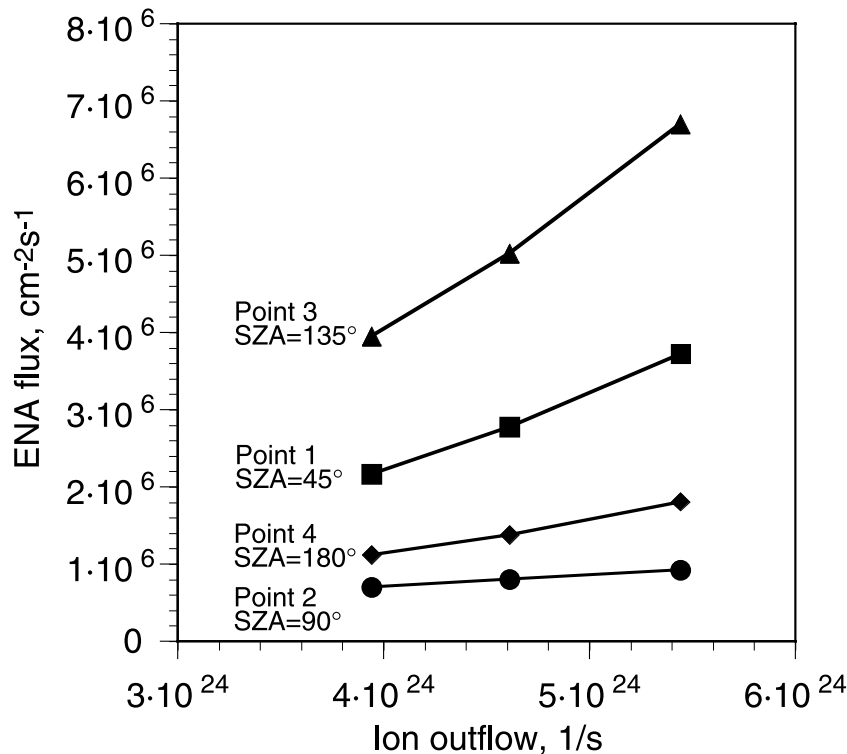
Figure 7. Dependence of the total ENA flux at the different vantage points shown in Figure 5 on the total ion outflow. The cold oxygen exospheric temperature was varied by 20% near the nominal value corresponding to the ion outflow 4.6×10^{24} s^{-1}.

mal) oxygen component results in a 14%−18% change in the ion outflow.

[29] It is indeed the cold component that is responsible for providing the majority of the oxygen ions escaping the system even though the ion production rate per one atom is higher for the hot component because the parameter $\tau_I^{hot} \gg \tau_I^{cold}$ in (7). Such a result has at least one evident explanation: the total amount of cold oxygen component contained between the heights $h = 210$ km and $h = R_m$ is 1.1×10^{17} atoms, but the hot oxygen population contained in this volume is just 1.4×10^{15} atoms. On the other hand, if the upper boundary of the obstacle is moved up to $h = 310$ km both populations become of the same order of magnitude, 6.2×10^{15} and 1.3×10^{15} respectively. Thus the result can be quite sensitive to the penetration depth of the electric field induced by the solar wind flow, that is $h = 210$ km in our model.

[30] Figure 7 shows the dependence of the total ENA flux at the different vantage points as a function of the total ion outflow calculated for different exospheric temperatures of the cold oxygen component. Since the variation in the ion density is small, the response in the ENA flux is linear. The strongest variations are observed at the point 3 at the $SZA = 135°$.

6. Discussion

[31] By solving the Vlasov equation numerically we obtained the oxygen ion distribution function. It shows a very strong asymmetry of a factor of 1000 in the column number density associated with the direction of the inter-

planetary electrical field (the asymmetry factor will be less for the number density). This is a purely kinetic effect not visible in MHD simulations [e.g., *Liu et al.*, 2001] since the electric field ions born in the $-Z$ hemisphere simply do not have enough room to make even a single turn in their gyromotion before they are lost in the dense upper atmosphere. They spend too short a time in the system to build up a substantial density. This strong asymmetry develops clearly in the corresponding ENA images (Figure 5, point 4). Here it comes, however, not only from the difference in the ion density but also from the direction of the particle motion. Ions in the $-Z$ hemisphere are at the beginning of their cycloidal motion and move approximately along the electric field. The associated ENA fluxes can not reach the vantage point in the tail. Therefore the interpretation and quantitative analysis of the asymmetry on the ENA images requires more detailed studies.

[32] One important remark should be made here. The plasma flow model used in these simulations is an axissymmetrical one and does not take into account any anomalies in the shape of the obstacle. The local magnetization [*Acuña et al.*, 1998] can break the symmetry and may affect the ENA image morphology. This will not, however, significantly change the ENA flux evaluation because it would affect the flow pattern only locally.

[33] Another kinetic feature is a jet of ions emitted from the subsolar point. A similar pattern has also been observed in hybrid simulations of a cometary environment [*Hopcroft and Chapman*, 2001] and test particle simulations of the ion wake of Mars based on a gas dynamic model [*Luhmann*, 1990]. Near the subsolar point the magnetic field is weaker

($\approx 2B_{sw}$) than in the other domains of the near-Mars space since the field lines are strongly "stretched" near this point [see *Kallio*, 1996, Figure 9]. The flow velocity, however, is not zero ($\approx 0.2V_{sw}$). Since the region size is small, even a relatively weak electrical field produced there is enough to bring the ions into the area of the strong interplanetary electric field. The production of oxygen ions is highest near the subsolar point because of the highest neutral density. This appears as a jet of ions coming from this region. The jet looks like a hot spot on the ENA images from the vantage points above the subsolar region, points 1 and 2 in Figure 5.

[34] Figure 3 shows the extension of the high density region of the $+Z$ hemisphere into the tail as seen in the projection onto the *OXZ* plane. The bright pixels in the upper part of the ENA image from the point 4 (Figure 5) indicate that this population moves tailward. This flow appears to be the main channel of the ion outflow. Indeed, the oxygen plasma with a density of 5 cm^{-3} as estimated from the column density distribution moves through a target area of $0.5R_m \times 1R_m$ with a velocity of 110 km/s corresponding to 1 keV. This builds up an escaping flux of 3×10^{24} particle/s that is close to the total outflow flux through the entire simulation box. The exact integration over the target area $4R_m \times 4R_m$ centered at $X = -2R_m$ and perpendicular to the *OX* axis gives 3.4×10^{24} particles/s accounting for 2/3 of the total escape number 4.6×10^{24} s^{-1}.

[35] The vantage points 3 and 4 are the most suitable ones to cover the ENA emissions associated with the tailward outflow, the main region of the ion outflow. Point 3 is the most sensitive to the variation in the outflow (Figure 7). This should be taken into account for optimizing the strategy of the ENA observations.

[36] For the solar minimum conditions the fluxes of the oxygen ENAs reach 10^5 cm^{-2}s^{-1}sr^{-1}eV^{-1} in the energy range $0.1-1.7$ keV. These fluxes are close to ones observed by the Low Energy Neutral Atom experiment on the IMAGE satellite from the polar outflow at the Earth [*Moore et al.*, 2001]. Indeed, for the quiet time *Moore et al.* [2001] estimate the directional oxygen ENA flux in the energy range of several tens eV associated with the ion outflow from the Earth's polar ionosphere to be around $(1-2) \times 10^8$ cm^{-2}s^{-1}sr^{-1}. In our case of an energy band of 1000 eV we also arrive at a flux of 10^8 cm^{-2}s^{-1}sr^{-1}.

[37] It was shown that almost half of all newborn ions experience charge exchange with the gases of the upper atmosphere. This has three important implications for the analysis of the solar wind interaction effects on the Martian atmosphere. First of all, oxygen atoms provide an extra contribution to the oxygen flux precipitating onto the Martian atmosphere. *Luhmann and Kozyra* [1991] showed that the precipitation of the oxygen ions induces atmospheric sputtering and may be a significant factor for the atmospheric erosion. The sputtered oxygen atoms will also modify the hot oxygen corona adding an extra energetic population [*Leblanc and Johnson*, 2001]. The oxygen ENA precipitation will enhance these processes. Secondly, the calculations of the oxygen escape rate should take into account charge-exchange losses along trajectories. Since nonresonance charge exchange remove oxygen ions from the total oxygen flow, the ion outflow may be smaller provided a newborn ENA will not escape the system.

Finally, the oxygen ENAs escaping the system carry away a substantial energy. The deceleration of the solar wind due to mass loading will be increased because an escaping oxygen atom leaves behind a cold oxygen ion (resonance charge exchange) which will again mass load the solar wind flow.

7. Conclusions

[38] We performed, for the first time, simulations of the oxygen ENA production at Mars. Our goals were (1) to qualitatively evaluate the effects of charge exchange on the oxygen ion population, (2) to calculate the oxygen ENA fluxes, (3) to simulate ENA images to understand their morphology within the chosen interaction model, and (4) to understand the relations between oxygen ENA fluxes and oxygen ion escape rate.

[39] About 50% of all oxygen ions originating from the photoionization of the oxygen exosphere experience charge exchange and are converted to ENAs. This produces very intense oxygen atom emissions as well as oxygen atom precipitation on the Martian upper atmosphere. It was established that for solar minimum conditions the fluxes of the oxygen ENAs reach 10^5 cm^{-2}s^{-1}sr^{-1}eV^{-1} in the energy range $0.1-1.7$ keV. The majority of oxygen ENAs have energies below 600 eV. For these energies the integral flux is up to 10^4 cm^{-2}s^{-1}eV^{-1}. This makes ENA imaging of the O$^+$ ions feasible. The morphology of the ENA images is defined by the structure of the oxygen ion distribution. All main features present in the parent ion distribution such as asymmetry, subsolar jet, tailward flow, are clearly visible on the images. However, the directionality of the ion motion strongly affects the ENA images. Vantage points within the plane containing the interplanetary electric field vector are the best for obtaining details of the parent ion distribution. The total ENA flux observed at a single vantage point depends on the total amount of oxygen ions in the system and may be used to obtain the instantaneous total ion flux escaping the planet.

[40] At this stage we have not considered the inversion techniques that would allow us to reconstruct the parent ion distributions. The parameterization of the interaction model that can be used for the inversion of solar wind ENA images [*Holmström et al.*, 2002] does not seem to be applicable in this case because of the unrealistic requirements for solving the Vlasov equation for each iteration of the parameters. One should consider either nonparametric approaches such as extending the ion distribution function in a system of orthogonal scalar functions, or directly parameterizing the distribution function. The later seems rather difficult taking into account the complicated morphology of the parent ion distribution.

[41] In the present study we used a simplified approach that is based on the axis symmetrical model and we do not take into account other ionization channels such as charge exchange and electron impact ionization. We also assumed that the upstream parameters are stable over the time it takes for the system to achieve its steady state and the time it takes for the slowest oxygen ENAs to propagate to the detector. The former is about a minute and the later is on the order of 5 min, the time an oxygen atom with an energy of 100 eV moves over a distance of $2R_m$. In future studies, the

effects induced by the local magnetizations should be taken into account. It would also be of interest to investigate the matter and energy transfer associated with the oxygen ENAs precipitating onto the Martian upper atmosphere and to compare these with the effects caused by the precipitation of O^+ pick-up ions [*Luhmann and Kozyra,* 1991].

References

Acuña, M. H., et al., Magnetic field and plasma observations at Mars: Initial results of the Mars Global Surveyor Mission, *Science*, *279*, 1676–1680, 1998.

Amsif, A., J. Dandouras, and E. C. Roelof, Modeling the production and the imaging of energetic neutral atoms from Titan's exosphere, *J. Geophys. Res.*, *102*, 22,169–22,181, 1997.

Barabash, S., R. Lundin, T. Zarnowiecki, and S. Grzedzielski, Diagnostic of energetic neutral particles at Mars by the ASPERA-C instrument for the Mars-96 mission, *Adv. Space Res.*, *16*, 81–86, 1995.

Barabash, S., J. Gimholt, and R. Lundin, The analyzer of space plasmas and energetic neutral atoms (ASPERA-3) for the Mars express mission, in *Proceedings of the Workshop on Energetic Neutral Atom Imaging of the Martian Environment, Kiruna, Sweden, September 2–3, 1998, IRF Sci. Rep. 248*, pp. 36–44, Inst. för Rymdfysik, 1998.

Barabash, S., A. Lukyanov, P. C. Brandt, and R. Lundin, Energetic neutral atom imaging of Mercury's magnetosphere, 3, Simulated images and instrument requirements, *Planet. Space Sci.*, *49*, 1685–1692, 2001.

Burch, J. L., et al., Views of Earth's magnetosphere with the IMAGE satellite, *Science*, *291*, 619–624, 2001.

Chamberlain, J. W., Planetary coronae and atmospheric evaporation, *Planet. Space Sci.*, *11*, 901–960, 1963.

Fox, J. L., J. F. Brannon, and H. S. Porter, Upper limits to the nightside ionosphere of Mars, *Geophys. Res. Lett.*, *20*, 1391–1394, 1993.

Hodges, R. R., Jr., Distribution of hot oxygen for Venus and Mars, *J. Geophys. Res.*, *105*, 6971–6981, 2000.

Holmström, M., S. Barabash, and E. Kallio, Energetic neutral atoms at Mars, 1, Imaging of solar wind protons, *J. Geophys. Res.*, *107*, doi:10.1029/2001JA000325, in press, 2002.

Hopcroft, M. W., and S. C. Chapman, 2D hybrid simulations of the solar wind interaction with a small comet in high Mach number flows, *Geophys. Res. Lett.*, *28*, 1115–1118, 2001.

Goldstein, R., D. Y. Young, H. Balsiger, F. Buehler, B. E. Goldstein, M. Neugebauer, H. Rosenbauer, R. Schwenn, and E. G. Shelley, Hot ions observed by the Giotto ion mass spectrometer at the comet P/Halley contact surface, *Astron. Astrophys.*, *187*, 220–224, 1987.

Kallio, E., An empirical model of the solar wind flow around Mars, *J. Geophys. Res.*, *101*, 11,133–11,147, 1996.

Kallio, E., and H. Koskinen, A test particle simulation of the motion of oxygen ions and solar wind protons near Mars, *J. Geophys. Res.*, *104*, 557–579, 1999.

Kallio, E., H. Koskinen, S. Barabash, R. Lundin, O. Norberg, and J. G. Luhmann, Proton flow in the Martian magnetosphere, *J. Geophys. Res.*, *99*, 23,547–23,559, 1994.

Kallio, E., J. G. Luhmann, and S. Barabash, Charge exchange near Mars: The solar wind absorption and energetic neutral atom production, *J. Geophys. Res.*, *102*, 22,183–22,197, 1997.

Kim, J., A. F. Nagy, J. L. Fox, and T. E. Cravens, Solar cycle variability of hot oxygen atoms at Mars, *J. Geophys. Res.*, *103*, 29,339–29,342, 1998.

Krasnopolsky, V. A., and G. R. Gladstone, Helium on Mars: EUVE and PHOBOS data and implications for Mars' evolution, *J. Geophys. Res.*, *101*, 15,765–15,772, 1996.

Leblanc, F., and R. E. Johnson, Sputtering of the Martian atmosphere by solar wind pick-up ions, *Planet. Space Sci.*, *29*, 645–656, 2001.

Lichtenegger, H. I. M., and E. Dubinin, Model calculations of the planetary ion distribution in the Martian tail, *Earth Planets Space*, *50*, 445–452, 1998.

Lichtenegger, H., H. Lammer, and W. Stumptner, Energetic neutral atoms at Mars, 3, Flux and energy distribution of planetary energetic H atoms, *J. Geophys. Res.*, *107*, doi:10.1029/2001JA000322, in press, 2002.

Lindsay, B. G., D. R. Sieglaff, K. A. Smith, and R. F. Stebbings, Charge transfer of keV O^+ ions with atomic oxygen, *J. Geophys. Res.*, *106*, 8197–8203, 2001.

Liu, Y., A. F. Nagy, T. I. Gombosi, D. L. DeZeeuw, and K. G. Powell, The solar wind interaction with Mars: Results of three-dimensional three-species MHD studies, *Adv. Space Res.*, *27*, 1837–1846, 2001.

Luhmann, J. G., A model of the ion wake of Mars, *Geophys. Res. Lett.*, *17*, 869–872, 1990.

Luhmann, J. G., and J. U. Kozyra, Dayside pickup oxygen ion precipitation at Venus and Mars: Spatial distributions, energy deposition, and consequences, *J. Geophys. Res.*, *96*, 5457–5467, 1991.

Luhmann, J. G., and K. Schwingenschuh, A model of the energetic ion environment of Mars, *J. Geophys. Res.*, *95*, 939–945, 1990.

Lundin, R., A. Zakharov, R. Pellinen, H. Borg, B. Hultqvist, N. Pissarenko, E. M. Dubinin, S. V. Barabash, I. Liede, and H. Koskinen, First measurements of the ionospheric plasma escape from Mars, *Nature*, *341*, 609–612, 1989.

Lundin, R., E. M. Dubinin, H. Koskinen, O. Norberg, N. F. Pissarenko, and S. V. Barabash, On the momentum transfer of the solar wind to the Martian topside ionosphere, *Geophys. Res. Lett.*, *18*, 1059–1062, 1991.

McKay, C. P., and C. R. Stoker, The early environment and its evolution on Mars: Implications for life, *Rev. Geophys.*, *27*, 189–214, 1989.

Moore, T. E., et al., Low energy neutral atoms in the magnetosphere, *Geophys. Res. Lett.*, *29*, 1143–1146, 2001.

Mura, A., A. Milillo, S. Orsini, E. Kallio, and S. Barabash, Energetic neutral atoms at Mars, 2, Energetic Neutral Atom production near Phobos, *J. Geophys. Res.*, *107*, 10.1029/2001JA000328, in press, 2002.

Perez-de-Tejada, H., Solar wind erosion of the Mars early atmosphere, *J. Geophys. Res.*, *97*, 3159–3167, 1992.

Phaneuf, R. A., R. K. Janev, and M. S. Pindzola, Collisions of carbon and oxygen ions with electrons, H, H_2, and He, *Rep. ORNL-6090*, vol. 5, Oak Ridge Nat. Lab., Oak Ridge, Tenn., Feb. 1987.

Roelof, E. C., Energetic Neutral atom image of a storm-time ring current, *Geophys. Res. Lett.*, *14*, 652–655, 1987.

Rosenbauer, H., et al., Ions of Martian origin and plasma sheet in the Martian magnetosphere: Initial results of the TAUS experiment, *Nature*, *341*, 612–614, 1989.

Torr, M. R., and D. G. Torr, Ionization frequencies for solar cycle 21: Revised, *J. Geophys. Res.*, *90*, 6675, 1985.

Torr, M. R., J. C. G. Walker, and D. G. Torr, Escape of fast oxygen from the atmosphere during geomagnetic storm, *J. Geophys. Res.*, *79*, 5267, 1974.

Verigin, M. I., et al., Ions of planetary origin in the Martian magnetosphere (Phobos 2/TAUS experiment), *Planet. Space Sci.*, *39*, 131–137, 1991.

Williams, D. J., E. C. Roelof, and D. G. Mitchell, Global magnetospheric imaging, *Rev. Geophys.*, *30*, 183–208, 1992.

Zhang, M. H. G., J. G. Luhmann, S. W. Bougher, and A. F. Nagy, The ancient oxygen exosphere of Mars: Implications for atmosphere evolution, *J. Geophys. Res.*, *98*, 10,915–10,923, 1993.
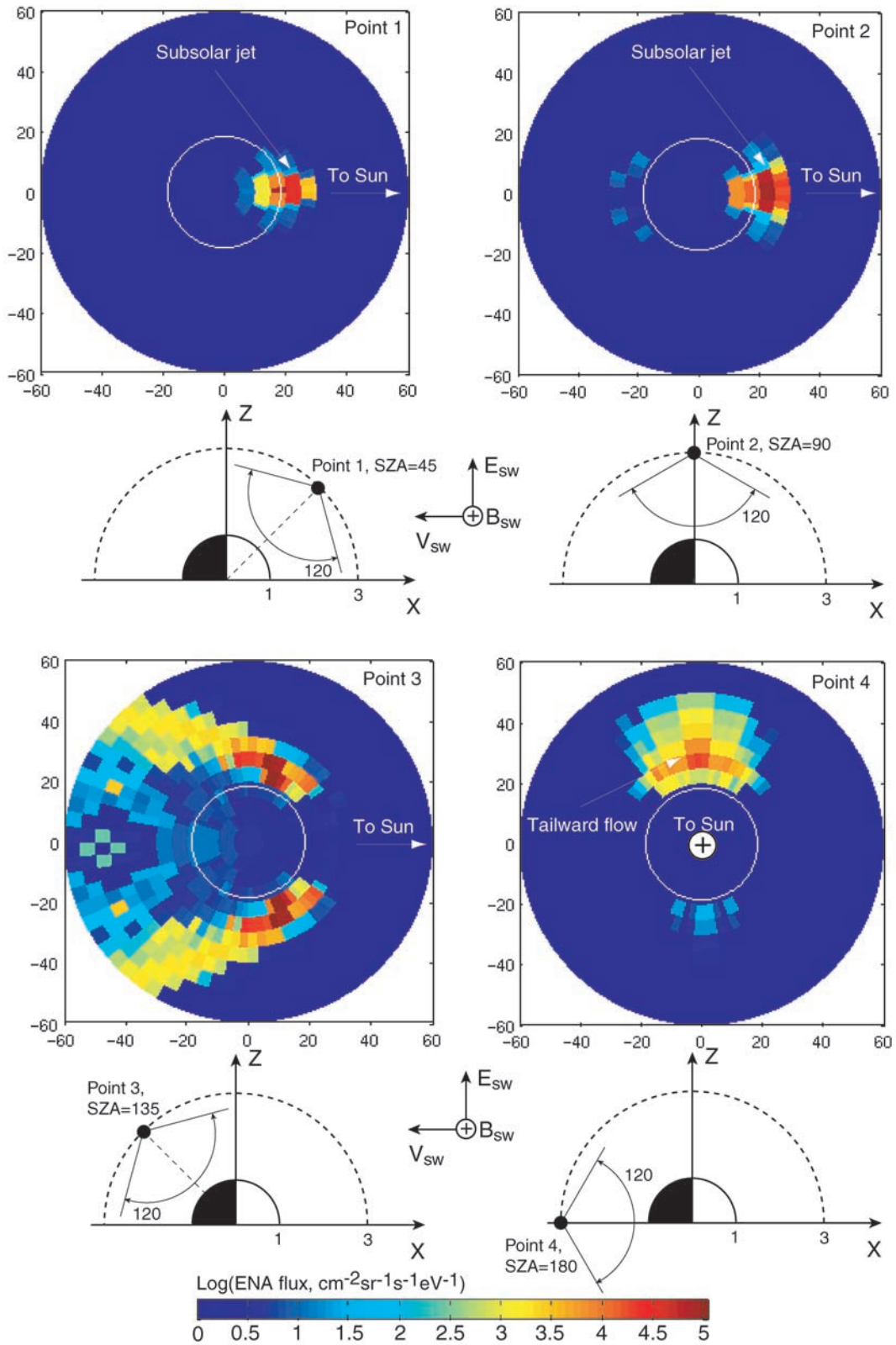
———————

S. Barabash and M. Holmström, Swedish Institute of Space Physics, P.O. Box 812, SE-98128 Kiruna, Sweden. (stas@irf.se; matsh@irf.se)

E. Kallio, Finnish Meteorological Institute, Geophysical Research, P.O. Box 503, FIN-00101 Helsinki, Finland. (Esa.Kallio@fmi.fi)

A. Lukyanov, Coventry University, Priory Street, Coventry CV1 5FB, UK. (csx212@coventry.ac.uk)
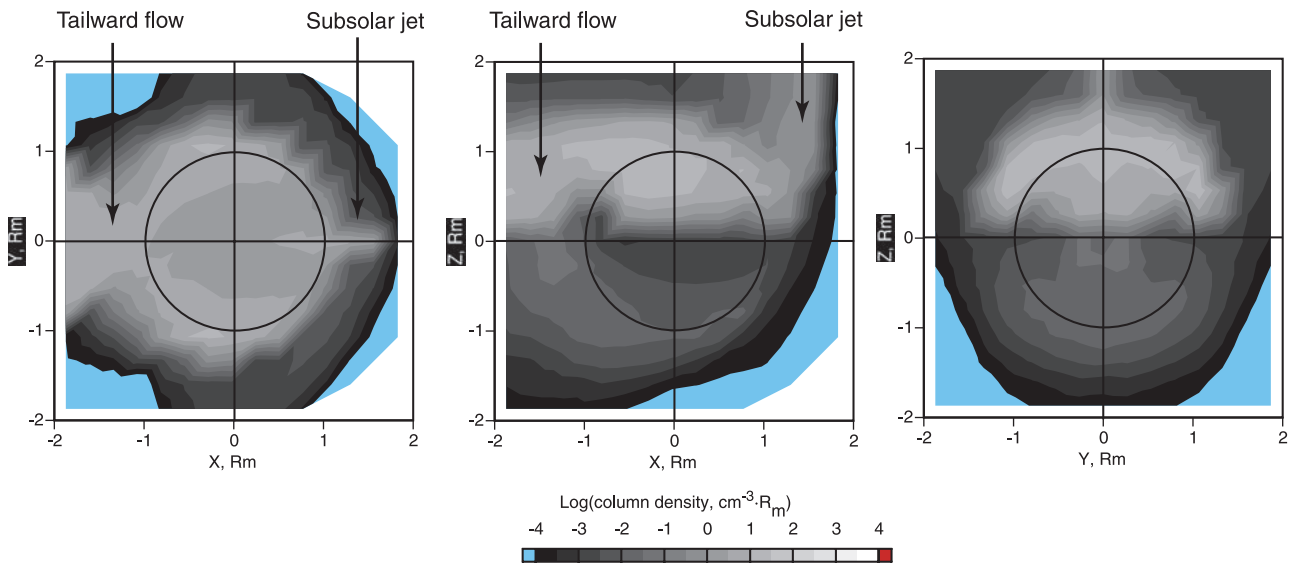
Figure 3. Oxygen ion column density distribution in the units $cm^{-3} \times R_m$ (3.39×10^8 cm^{-2}) in solar ecliptic coordinates. The solar wind magnetic field is 2 nT and directed along the OY axis. The corresponding convection electric field is along OZ. The solar wind velocity is directed along the $-X$ axis and is equal to 500 km/s.

Figure 5. ENA images for vantage points with different solar zenith angles (SZA). The energy range: 0.1–1.65 keV. The position of the vantage points are shown in the inserts as well as electrical and magnetic field vectors. All points are in the *OXZ* plane.